Numerical simulation for viscous free-surface flows for reverse roller-coating

M.S. Chandio and M.F. Webster
Institute of non-Newtonian Fluid Mechanics, Department of Computer Science, University of Wales, Swansea, UK

Keywords *Free form surfaces, Numerical simulation, Finite elements*

Abstract *This article is concerned with the numerical simulation of a reverse roller-coating process, which involves the computation of Newtonian viscous incompressible flows with free-surfaces. A numerical scheme is applied of a transient finite element form, a semi-implicit Taylor-Galerkin/pressurecorrection algorithm. For free-surface prediction, we use kinematic boundary adjustment with a mesh-stretching algorithm. In the present work, an alloy sheet (foil) passes over a large roller and then a smaller applicator roller, which provides the in-feed. In combination, the applicator roller, the foil and the fluid form part of the underside coating mechanism. The aim of this study is to investigate fundamental aspects of the process, to ultimately address typical coating instabilities. These may take the form of chatter and starvation. A uniform coating thickness is the desired objective. A mathematical model is derived to describe the solvent coating applied to the underside of the sheet, assuming that the lacquer is a Newtonian fluid. In particular, the work has concentrated on the flow patterns that result and a parameter sensitivity analysis covering the appropriate operating windows of applied conditions. Effects of independent variation in roll-speed and foil-speed are investigated, to find that maxima in pressure, lift and drag arise at the nip and are influenced in a linear fashion.*

1. Introduction

In this study the effectiveness of finite element modelling is investigated to predict the flow associated with the reverse roller-coating of alloy sheets using a protective film of solvent-based lacquer. A mathematical model is derived to describe the coating applied to the underside of the foil sheet, assuming that the lacquer is a Newtonian fluid. In particular, the work has concentrated on the flow patterns that result and a parameter sensitivity analysis covering appropriate operating windows of applied conditions. This covers variation in application roll-speed and foil-speed, and consideration of flow conditions in the nip region. A finite element simulation of the roller-coating process is presented, based on a semi-implicit Taylor-Galerkin/Pressure-correction algorithm (Townsend and Webster, 1987; Hawken *et al.*, 1990; Carew *et al.*, 1993).

International Journal of Numerical Methods for Heat & Fluid Flow, Vol. 12 No. 4, 2002, pp. 434-457.

DOI 10.1108/09615530210433288

Author for correspondence, Institute of Non-Newtonian Fluid Mechanics, Department of Computer Science, University of Wales Swansea, Singleton Park, Swansea SA2 8PP, UK, E-mail: M.F.Webster@swan.ac.uk

Viscous flow with free-surfaces is common and arises in many important industrial application areas, particularly in coating and printing situations. In the literature, flows between pairs of rolls have been extensively studied (Fourcade *et al.*, 1999; Cohu and Magnin, 1997; Carvalho and Scriven, 1997; Carvalho and Scriven, 1997; Chen and Scriven, 1988; Benjamin, 1994), where a substrate is pressed between a set of contra or forward rotating rollers. The general requirement is to achieve a uniform coating thickness. It is reported in The literature would indicate that, high-pressure in the nip region generates instability in the flow, that subsequently affects the coating liquid layer, see Fourcade *et al.* (1999); Cohu and Magnin (1997); Carvalho and Scriven (1997); Carvalho and Scriven (1997); Chen and Scriven (1988). Similar findings are observed in this study, where pressure has an elevated value in the nip region. There is a sparsity of work in the open literature on reverse roller-coating between foil and roller. Hence, we first review work cited on roller-coating between two rollers. Fourcade *et al.* (1999) investigated a coating operation of a reverse roller-coating process between two rollers. The main attention is focused on the deformation of the elastomer on the coated roll. It is reported that the pressure increases in the converging section of the gap, and reaches its peak slightly to the left of the contact point of the rollers. The largest deformation of the elastomer cover of 70 mm is observed to occur at the location where the pressure reaches a maximum. The lower the gap size, the higher the pressure peak that is observed.

Cohu and Magnin (1997) conducted experimental investigations into forward roller-coating of Newtonian fluids between deformable rolls. These authors observed that the decrease of the thickness of a rubber cover on a roller, below a critical value, tends to decrease the coating thickness significantly. Carvalho and Scriven (1997) have argued in their numerical work, based on forward roller-coating, that the upstream free-surface touches the top roll, and air is trapped between the roll surface and the coating liquid. Consequently the coated film that is delivered is defective. Various flow states are described, both metered and premetered, by moving the rolls apart and bringing them together. As the rolls are pushed together, the gyre moves upstream towards the inlet plane. These authors have replaced the fixed inlet film thickness condition with a weighted kinematic residual that guarantees the flow is normal to the inlet boundary in an integral sense.

Carvalho and Scriven (1997) investigated the effect of soft-roll deformation with respect to the onset of ribbing on the coated liquid layer. Their main findings showed how a deformable cover may be used to lessen the ribbing on the liquid layer to achieve a required coating thickness. They found that in forward-roller coating, deformation influenced gap geometry and this generated ribbing on the liquid layer, on each of the roll surfaces at high roller speeds. They also analysed time-dependent response to infinitesimal transverse disturbances. A mathematical model was presented to predict the

critical capillary number for the onset of ribbing. They concluded that roll cover deformation alters the wavelength of the ribbing pattern. Roll cover softness is related to increasing the solids elasticity number. Increasing the elasticity number of the soft-roll cover makes the ribbing pattern wavelengths larger and wave numbers smaller; this stimulates the fastest instability modes. The consequence is a larger ribbing wavelength and consequently an extended period to achieve a level film.

It is necessary to consider the state of inflow to provide appropriate flow conditions, stipulating flow rate and profile form. According to Benjamin (1994), in meniscus coatings, the flow is always pre-metered and therefore imposing a plug-velocity profile at the inflow boundary is a satisfactory boundary condition. Hence, we follow this thinking, as do Chen and Scriven (1988) likewise. This implies that we adopt a constant inflow rate, as delivered by the premetering. Largely, this flow rate is determined by that at outflow, based upon a known film-speed and thickness.

For the last two decades the finite element method has played an important role in simulating the flow of fluids subject to free surfaces. Literature of relevance on this topic can be found in Keunings (1986); Sizaire and Legat (1997); Tanner *et al.* (1975); Silliman and Scriven (1980); Saito and Scriven (1981); Ramaswamy (1990); Hirt *et al.* (1974); Sato and Richardson (1994); Ding *et al.* (1993); Regalt *et al.* (1993). One difficulty with computer modelling of such coating scenarios, lies in the treatment of moving free-surface problems, accommodating kinematic and dynamic boundary conditions (Keunings, 1986) on the free-surface and the simultaneous calculation of its position. Sizaire and Legat (1997) have adopted an approach similar to that of Keunings (1986) for the treatment of free-surface boundaries, within the viscoelastic regime.

Tanner *et al.* (1975), constructed a Galerkin finite element scheme for computing free surfaces with the use of the kinematic condition. Drawbacks to this approach are commented upon by Silliman and Scriven (1980) who argue that such a choice is expensive to implement and relies heavily upon the initial guess. Furthermore, such kinematic conditions alone will not provide an efficient way to update the free surface in stagnant regions. This technique is suitable only when surface tension effects dominate viscous effects.

Saito and Scriven (1981) have illustrated a particular strategy to represent the free-surface position, referencing the meniscus section with the polar arm of length $f(\theta)$ and flat sections by height $h(x)$. This introduces a new degree of freedom on each free-surface node that corresponds to the nodal position. A variant of this is advocated in the present study, as this is taken to be most suitable for the present requirements. A corresponding Petrov-Galerkin formulation is derived for free-surface location and the subsequent adjustment of the original mesh. This allows for local point wise corrections that may supplement the solution procedure and invoke remeshing locally, if required.

Generally, Eulerian techniques are used to compute the field variables at fixed nodal points of the mesh. A separate system of equations is generated for the free surface location. These schemes are suitable even with meshes that see large distortions. Lagrangian approaches localize the fluid location properties to a finite number of particles that move with the fluid. This approach fails when distortions are large. Ramaswamy (1990) has presented an arbitrary Lagrangian-Eulerian finite element technique, similar to that of Hirt *et al.* (1974). In the Lagrangian section, the mesh velocity equates to the fluid velocity, that removes the convective fluxes from the momentum transport equation. In this manner, nodal point location may be computed via a velocity-correction scheme. Subsequently, the mesh velocity is updated using these nodal point locations. In the Eulerian phase, convective fluxes are evaluated. Finally, an updated position of the free-surface is computed, using both fluid and mesh velocities. A conventional Galerkin-Bubnov finite element method is employed. This mixed Lagrangian-Eulerian method (Ramaswamy, 1990) takes advantage of these aspects and mitigates any mesh distortion difficulties that may arise during the Lagrangian phase.

Sato and Richardson (1994) proposed a fringe element generation method based upon a hybrid finite element/finite volume method. There is no global remeshing performed with this method. Instead, the fluid flows over a fixed mesh wetting new portions. New fringe elements are created in the surface neighbourhood, conforming to the original mesh structure. In contrast to local remeshing/stretching methods, such an approach avoids mesh distortion. Each element and node is assigned a dry-wet Boolean flag to identify whether it is wetted by the fluid or not. Starting from the nodal flag information, the new location of the free surface at time t^{n+1} is traced via kinematics considerations, based on an Euler scheme. A similar strategy is adopted by Ding *et al.* (1993) for the computation of moving free-surface boundaries. Regalt *et al.* (1993) used a nodal displacement scheme with a combination of remeshing of the flow domain for a dip coating process. Since the free surface position is not known apriori and if its initial guess is far from the actual solution, then it is observed in Regalt *et al.* (1993) that the use of kinematic boundary conditions directly lead to convergence difficulties. In order to force the search procedure to converge with this scheme, the kinematic boundary conditions were under-relaxed, during the first few iterations.

The present work introduces new aspects of implementation, based on the ideas of Saito and Scriven (1981) for the computation of free-surfaces. This scheme is not restricted to a particular shape. Rather it can be transformed from one coordinate system to another, locally or globally, according to the free-surface orientation and domain. The method is tested on the complex flow section, described below in Figure 1, that contains both flat and curved meniscus shapes. The flow zone comprises of the inflow on the roller, passing

to the nip between roller and foil, and the coating flow, from the meniscus to the outflow on the foil.

2. Governing equations

For an incompressible and isothermal laminar flow, the system of governing equations may be described by momentum and the continuity equations. In the absence of body forces, the system may be expressed in the form

$$\rho \frac{\partial u}{\partial t} = \nabla \cdot T - \rho u \cdot \nabla u - \nabla p \tag{1}$$

$$\nabla \cdot u = 0 \tag{2}$$

where ρ is the fluid density, t is the time, $u(x,t)$ is the fluid velocity and p is the isotropic pressure. For Newtonian flows, the stress $\boldsymbol{T}$ is defined via a Newtonian viscosity μ, and the rate of deformation tensor $\boldsymbol{D}$,

$$T = 2\mu \boldsymbol{D} \tag{3}$$

where

$$\boldsymbol{D} = \frac{L + L^t}{2} \quad \text{and} \quad L^t = \nabla u. \tag{4}$$

With a constant viscosity and using the continuity equation (2), the Navier-Stokes equation can be recovered,

$$\rho \frac{\partial u}{\partial t} = \mu \nabla^2 u - \rho u \cdot \nabla u - \nabla p \tag{5}$$

where $\mu \nabla^2 u$ is the diffusion term.

Adopting characteristic scales on velocity, U, length, L and viscosity, μ, we may define non-dimensional variables $u = Uu^*$ and $p = [\mu U/L]p^*$. Hence, we may define an equivalent non-dimensional system of equations to (5) and (2), discarding the * notation for convenience of representation,

$$\begin{aligned} \mathrm{Re} \frac{\partial u}{\partial t} &= \nabla^2 u - \mathrm{Re}\, u \cdot \nabla u - \nabla p, \\ \nabla \cdot u &= 0, \end{aligned} \tag{6}$$

where the non-dimensional group Reynolds number is defined as $\mathrm{Re} = \rho UL/\mu$.

For the solution of the given system of governing equations, both initial and boundary conditions are required. Initial conditions can be formed by prescribing initial values for the primitive field variables at $t = 0$,

$$U(x,t) = u_0(x,0),$$

$$p(x,t) = p(x,0).$$

Conditions at the free-surface require a normal constraint,

$$p + \tau_{nm} = -p_0 + \sigma\beta, \tag{7}$$

whilst the absence of friction ensures the tangential constraint,

$$\tau_{nt} = 0. \tag{8}$$

Here, τ_{nn}, τ_{nt} are normal and tangential stress components, respectively, p_0 is atmospheric and p local pressure, σ is a surface tension coefficient and β is the mean curvature of the free-surface (Chen and Scriven, 1988). The effects of surface tension are neglected in these calculations. On the free-surface boundary, the normal stress is equated to that of atmospheric pressure, which is taken as ambient ($p_0 = 0$) and the tangential stress should vanish, so the surface tension is zero. Remaining boundary conditions are taken of no-slip on roller and foil, uniform flow at inlet on the roller and outlet on the foil, with vanishing flux across the nip. This suffices to specify the problem.

3. Finite element analysis

The general procedure adopted is one of time-stepping to a steady-state solution. This approach may be used either in a true transient context or one simply to achieve steady-state. Here, we are interested primarily in steady conditions, though subsequently, we wish to consider transient instabilities. A Taylor-Galerkin algorithm is used to solve the governing equations (6). A twostep Lax-Wendroff approach, based on a Taylor series expansion up to second order in time, is used to find the solution at steady-state. A two-step pressurecorrection method is applied to handle the incompressibility constraint. Employing the Crank-Nicolson treatment on diffusive term, the resultingsolution method produces three fractional-staged (Hawken *et al.*, 1990).

In stage one non-solenoidal velocity field $u^{n+1/2}$ and u^* are computed via a predictor-corrector doublet. A Jacobi method is used to solve the resulting mass matrix equation. With the use of u^*, the second stage computes the pressure difference, $p^{n+1} - p^n$, via a Poisson equation, applying Choleski method. The third stage completes the loop, calculating the end-of-time-step solenodal velocity field u^{n+1} by Jacobi iterative solver. The details upon this implementation may be found in Townsend and Webster (1987) and Hawken *et al.* (1990).

Following the notation of Cuvelier *et al.* (1986), the velocity and pressure fields are approximated by $U(\mathbf{x}, t) = U^j(t)\phi_j(\mathbf{x})$ and $P(\mathbf{x}, t) = P^k(t)\varphi_k(\mathbf{x})$, where U and P represents the vector of nodal values of velocity and pressure respectively and ϕ_j is a piecewise quadratic and φ_k is a linear basis function.

On a specified field domain, the fully discrete semi-implicit Taylor-Galerkin/pressure-correction system of equations in matrix form is given as follows:

$$\text{Stage 1a.}\quad \left(\frac{2\mathrm{Re}}{\Delta t}M+\frac{1}{2}S\right)\left(U^{n+\frac{1}{2}}-U^{n}\right)=\{-[S+\mathrm{Re}N(U)]U+L^{T}P\}^{n}$$

$$\text{Stage 1b.}\quad \left(\frac{\mathrm{Re}}{\Delta t}M+\frac{1}{2}S\right)(U^{*}-U^{n})=(-[SU+L^{T}P]^{n}-[\mathrm{Re}N(U)U]^{n+\frac{1}{2}} \tag{9}$$

$$\text{Stage 2.}\quad K(P^{n+1}-P^{n})=-\frac{2}{\Delta t}\mathrm{Re}LU^{*}$$

$$\text{Stage 3.}\quad \frac{\mathrm{Re}}{\Delta t}M(U^{n+1}-U^{*})=\frac{1}{2}L^{T}(P^{n+1}-P^{n}),$$

where M, S, $N(U)$, L, and K are consistent mass matrix, momentum diffusion matrix, convection matrix, pressure gradient matrix and pressure stiffness matrix respectively. In matrix form, these can be expressed as follows:

$$M_{ij}=\int_{\Omega}\phi_i\phi_j\,\mathrm{d}\Omega,$$

$$N(U)_{ij}=\int_{\Omega}\phi_i\left(\phi_i U_1\frac{\partial\phi_j}{\partial x}+\phi_1 U_1\frac{\partial\phi_j}{\partial y}\right)\mathrm{d}\Omega,$$

$$((L_k)_{ij})=\int_{\Omega}\frac{\partial\phi_j}{\partial x_k}\,\mathrm{d}\Omega,$$

$$K_{ij}=\int_{\Omega}\nabla\psi_i\nabla\psi_j\,\mathrm{d}\Omega,$$

$$S_{ij}=\int_{\Omega}\nabla\phi_i\nabla\phi_j\,\mathrm{d}\Omega.$$

4. Free-surface location

Some of the difficulties, which arise in the mathematical modelling, are associated with the presence of a free-surface, whose position is unknown apriori and must therefore be computed as part of the scheme. In the first instance, the geometry of the free-surface is based on a set (estimated) initial position, see Figure 1. The coat-outlet flow on the foil is taken as uniform thickness (width of a_{outlet}, qualifies positions A and B). The same is true on the roller for inflow (gives D and E). The meniscus is specified on the basis of extremities B and D, and interconnecting arc through C. Guidance on the angle of location of meniscus from the nip, can normally be obtained by experiment. Here, the intersection of the angle bisector between foil and roller, with the polar arm to the origin is taken at an angle of 94°, establishing point C. Arcs BC

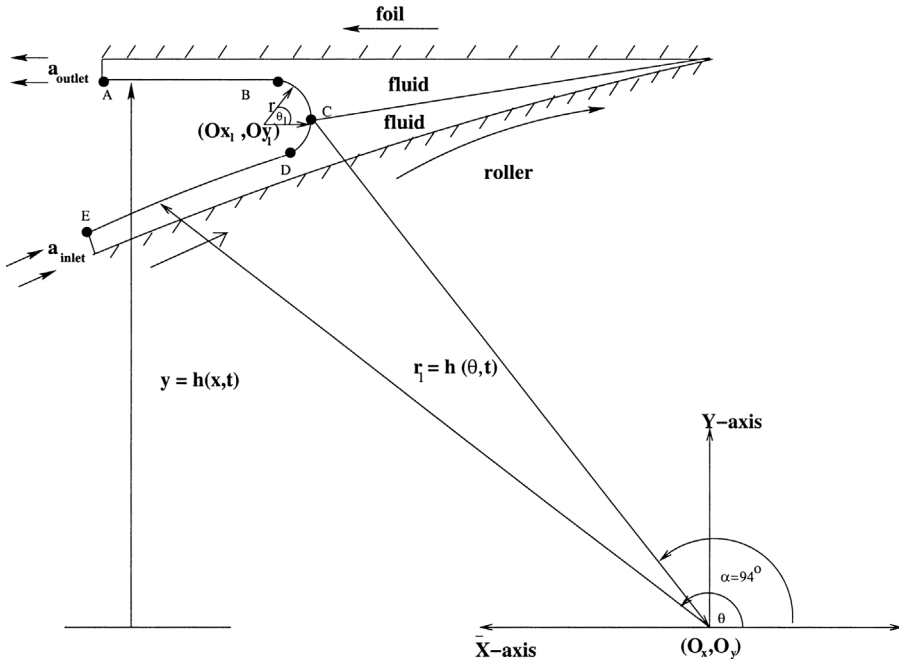

Figure 1.
Schematic flow diagram

and CD are then taken as circular arc segments, so that BC tangents the coating level and, likewise, CD tangents the roller inflow level (radius of arcs is then equally distant from B, C and D; this locates B and D precisely). A meniscus shape is sketched for illustration in Figure 1. The eventual position of the free-surface $h(x,t)$, is determined via solution of the following two equations:

On flat free-surface boundaries (lines at constant y):

$$\frac{\partial h}{\partial t} = -U_x \frac{\partial h}{\partial x} + U_y, \tag{10}$$

On the curved meniscus boundary section (lines at fixed azimuthal angle θ setting):

$$\frac{\partial h}{\partial t} = -U_\vartheta \frac{1}{r} \frac{\partial h}{\partial \vartheta} + U_r, \tag{11}$$

where the translation between Cartesian and polar coordinates is assumed.

Initial conditions for the transient algorithm are taken as quiescent upon the field, but with plug flow imposed at inflow and outflow. It is also found helpful, to enhance efficiency in convergence to a steady scenario, to first fix the free boundary as a solid surface (location as above) and compute an internal flow field from which to commence the free-surface solution. This provides a contrast to free-surface movement from a predefined position. With free-surface

movement, the new position of each node on the free-surface is computed using the above equations (10) or (11), according to the particular boundary section. Remeshing must be performed after each time-step to avoid excessive distortion of elements in the boundary zones.

In a general discrete variational form, equation (10) and (11) can be expressed in a fourth algorithmic stage to the time-step cycle:

$$\text{Stage 4} \quad \begin{aligned} &\frac{1}{\Delta t}\int_{\Gamma}(\psi_i + (\alpha_1 + u\cdot\nabla\psi_i))(\psi_k + (\alpha_2 + u\cdot\nabla\psi_k))\Delta H_{\mathrm{k}}^{n+1}\,\mathrm{d}\Gamma_F \\ &\quad - \int_{\Gamma}(\psi_i + (\alpha_1 + u\cdot\nabla\psi_i))u\cdot\nabla\psi_k H_{\mathrm{k}}^{n}\,\mathrm{d}\Gamma_F \end{aligned} \tag{12}$$

adopting notation for time-step, Δt, interpolant, $H^n(x)$, interpolating functions, $\psi_k(x)$, and nodal solution increment, ΔH_k^n,

$$H^n(x) = H_k^n\psi_k(x) \quad \text{and} \quad \Delta H_k^{n+1} = (H_k^{n+1} - H_k^n). \tag{13}$$

We utilise generalized scalar factors α_i to switch between Galerkin and SUPG (explicit and implicit) schemes, as and when required. A free-surface boundary segment is indicated by Γ_F, over which quadrature may be established. In equation (12), the generalized form of convective term is represented, subsuming either equation (10) or (11), depending upon the particular boundary segment under consideration. We have found it most effective to use $\alpha_1 = \alpha^h$ (an SUPG parameter (Carew *et al.*, 1993)) and $\alpha_2 = \Delta t/2$ to recover an implicit SUPG scheme. Then, both ψ_i (and ψ_k) are taken as linear functions on straight-sided boundary elements sections. In the present work, the free-surface location is computed by an SUPG approach. This is due to the dominant hyperbolic type of the corresponding equations (10–11), for which some form of upwinding is appropriate. This approach has accelerated solution convergence in comparison to a conventional Galerkin approach. In addition, we have the freedom of choice of free-surface time step size. Here, we have employed the same Δt for field and free-surface computations, as we are interested only in steady-state solutions. Elsewhere, when transient accuracy is important, we may take advantage of socalled pseudo-time-steps (Ding *et al.*, 1993; Nithiarasu and Zienkiewicz, 2000).

5. Problem specification

In the first instance, we confine attention to the model problem as illustrated in Figure 1. The problem is parameterised through coating thickness (characteristic length), foil speed, U_{foil}, (characteristic speed, typically $O(10^2)$), and rotation speed of the roller, U_{roll}, 90 per cent of the foil speed. A roller of radius r_1, rotates at angular rate ω (speed $U_{\mathrm{roll}} = \omega r_1$), applying a coating to the underside of the alloy sheet of thickness $h(x, t)$. The sheet rests on both the

roller and the thin film of fluid between the roller and the sheet. The sheet moves with speed U_{foil} in the horizontal direction (negative x) and the problem is posed in a Cartesian frame of reference. As a first approximation, there is no leakage assumed in the nip region and steady-state flow configurations are sought.

The system of governing equations, in conjunction with free boundary equations, in the absence of surface tension, is solved by employing a timemarching finite element semi-implicit Taylor-Galerkin/Pressure-correction algorithm (Townsend and Webster, 1987; Hawken *et al.*, 1990; Carew *et al.*, 1993), applying appropriate initial and boundary conditions. The mesh used is displayed in Figure 2 and has 2925 nodes, 1302 elements and 6662 degrees of freedom. Three distinct mesh views are displayed. Figure 2a is a full mesh view that clearly indicates the wide aspect ratios involved. Figure 2b and 2c provide zoomed sections of mesh at the meniscus region and towards the nip, accordingly.

Variation in roll speed covers settings of 90 per cent, 99 per cent, 108 per cent and 120 per cent of the standard foil speed, $\bar{U}_{\text{foil}}$, typically $O(10^2)$m/min. Similarly, variation in foil-speed is taken from $0.5^*\bar{U}_{\text{foil}}$ to $2.5^*\bar{U}_{\text{foil}}$ at increments of $0.5^*\bar{U}_{\text{foil}}$.

No-slip boundary conditions for the flow on solid surfaces are taken as:

$$\text{on the foil: } U_x = -\bar{U}_{\text{foil}}, U_y = 0;$$

$$\text{on the roller: } U_x = U_{\text{roll}} \cos\theta, U_y = U_{\text{roll}} \sin\theta;$$

where $U_{\text{roll}} = R\omega$, R is the radius and ω the angular rotation rate of the roller.

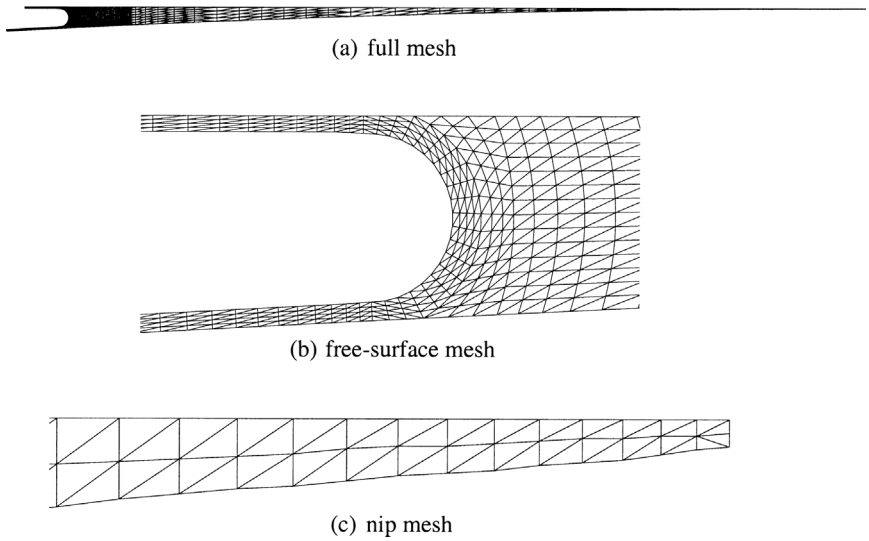

Figure 2.
Finite element mesh sections

On free-surface boundaries, conditions (7) and (8) apply, and there, pressure remains unspecified. Hence, once foil and roll-speeds have been set, there is a balance imposed between inflow and outflow, presuming there is no leakage at the nip. If we assume that the coating thickness is given (experimentally determined) and that a plug flow is generated both on the foil and roller, then the roller feed thickness is also set.

5.1 Lift and drag

Lift and drag are mechanical forces that arise between solid and liquid surfaces. Here we are concerned with the lift on the foil and the drag on the roller. For a Newtonian fluid the lift, drag and stress may be expressed through the following expressions:

$$L_{\text{foil}} = \int_{\Gamma_{\text{foil}}} \{ -p \sin\theta + \tau_{xy} \cos\theta + \tau_{yy} \sin\theta \} \, \mathrm{d}\theta = \int_{\Gamma_{\text{foil}}} L_{\text{f}} \, \mathrm{d}\theta \qquad (14)$$

$$D_{\text{roller}} = \int_{\Gamma_{\text{roller}}} \{ -p \cos\theta + \tau_{\text{xx}} \cos\theta + \tau_{xy} \sin\theta \} \, \mathrm{d}\theta = \int_{\Gamma_{\text{roller}}} (-D_{\text{R}}) \, \mathrm{d}\theta \qquad (15)$$

where $\tau = 2\mu D$; L_f and D_R are distributional lift and drag quantities.

6. Numerical results

The simulation results begin with the standard setting as discussed in section 5, that follows four sub-sections of study. The first is associated with the increment of roll-speed at fixed foil-speed. The second considers the effects upon the flow behaviour of variation in foil-speed at fixed roll-speed. Next we switch our attention to inlet flow instability on roller. Presentation of results is achieved through flow field representation of streamlines in the meniscus free-surface regions and pressure line contours in the nip region. At various flow settings, tabulations in pressure, shear-rate, and lift on the foil and drag on the roller are provided, from which we may infer certain properties of the flow. All values are reported in a non-dimensional form.

6.1 Flow patterns at standard settings

A standard foil-speed setting of 1 unit and roller speed, 90 per cent of foil-speed, constitutes the base scenario around which variations are subsequently sought. A steady-state solution is obtained, starting from rest, by imposing Dirichlet boundary conditions. Here, free boundary conditions refer to natural unconstrained forms, where boundary location is also determined. Fixed implies strong constrained boundary conditions on restrained boundary locations. When the boundaries are set as fixed, a flow reversal around the meniscus is apparent, see Figure 3a. Switching from fixed to free boundary settings, removes any flow reversal around the meniscus, see Figure 3b. So that

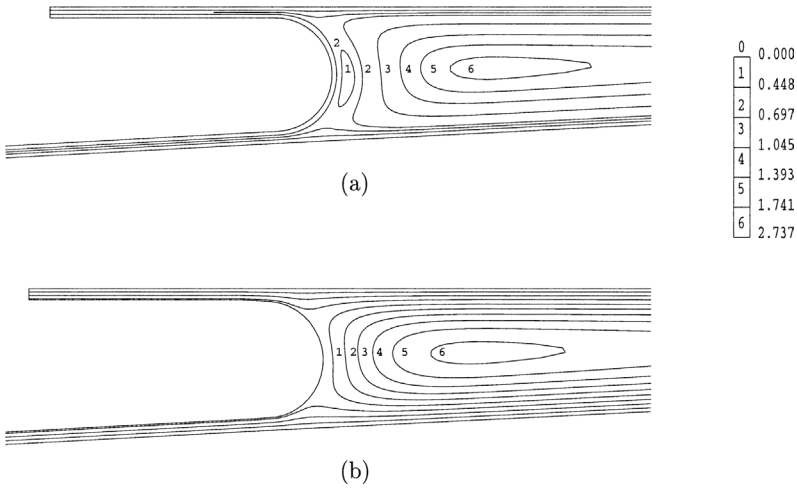

Figure 3.
Streamline patterns: a) fixed and b) free boundary conditions, $U_{\text{roll}} = 90\%\ \bar{U}_{\text{foil}}$

in the free-surface configuration, streamline patterns indicate that flow travels with the roller to the nip, before reversing and being taken up by the foil, to pass into the coating film on the sheet. A central long thin vortex is set up in the flow region between the roller and the foil, see Figure 3. Free boundary conditions apply to all calculations performed below.

6.2 Analysis with increasing roll-speeds

We study the streamline patterns that emerge in the meniscus region for speeds of 90 per cent, 99 per cent, 108 per cent and 120 per cent of foil-speed, see Figure 4, with ten contours per field plot from maximum at the vortex center to minimum at the meniscus. A slight distortion is observed of the streamline adjoining the meniscus, indicating a shift with dominance of foil over roll-speed initially at 90 per cent setting, to a balanced scenario at 99 per cent setting. The distortion is reversed for 108 per cent and 120 per cent settings. A single vortex has dominated the flow field at each speed setting, and the maximum magnitude of these streamlines increases with increasing roll-speed (Isaksson and Rigdahl, (1994) reported similar results).

Pressure maxima in the nip region are $O(10^6)$ units, and are gradually decreasing with linear trend as roll-speed increases, see Figure 5a. Foil distributional pressure (P_f) is shown in Figure 5b along the foil length. The pressure level is fairly low along most of the foil, rises significantly close to the nip and decreases with increasing roll-speed. However, the magnitude of these decreasing trends is small due to the small variation in roll-speeds. Therefore, insignificant changes in pressure line contours are observed for the different roll-speeds. Pressure line contours are included in Figure 5c for 90 per cent roll-speed of $\bar{U}_{\text{foil}}$. The region of maximum pressure broadens away from the nip as

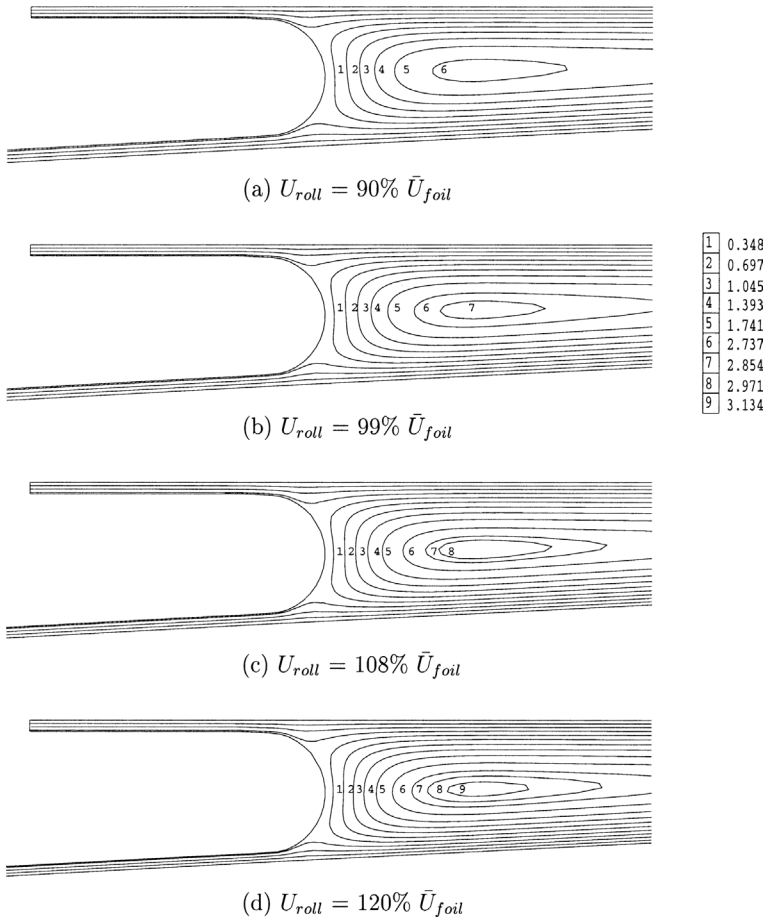

Figure 4.
Streamline patterns, increasing roll-speed

rollspeed increases. Likewise, maximum shear-rate is charted against increasing roll-speed setting in Table I, attaining values of $O(10^3)$ units in the nip region, see Figure 5a. Maxima in shear-rate shift from the foil at 90 per cent roll-speed, to a balanced pattern at 99 per cent roll-speed, and finally towards the roller at 108 per cent speed and above, see Figure 7. Since the locations of application of shear-rate maxima shift, from foil to roller with increasing roll-speed, it is no surprise that shearrates increase with roll-speed, see Table I. Inlet layer thickness a_{inlet} is taken relative to outlet, that is maintained at a constant level as speed of roller increases. Note, that due to pre-metering, a constant flow rate is assumed for all settings.

Lift (L_{foil}) on the foil and drag (D_{roller}) on the roller are charted correspondingly against roll-speed setting (see Table I, Figure 6). Lift on the foil is $O(10^7)$ units and decreases with increasing roll-speed, in contrast drag on

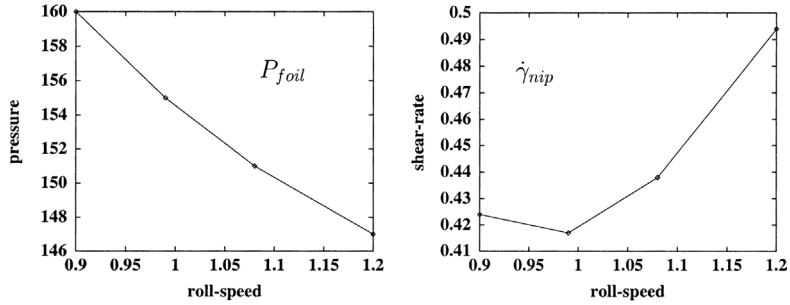

(a) Pressure and shear-rate line plots (values*10^3), increasing roll-speed

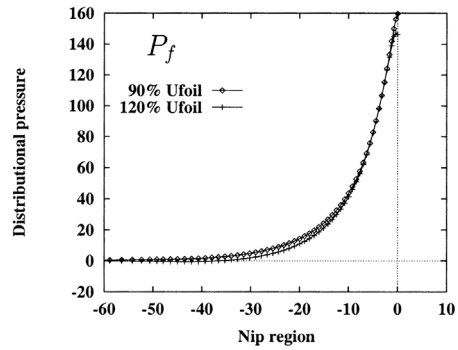

(b) Foil distributional pressure (P_f) values*10^3, towards the nip

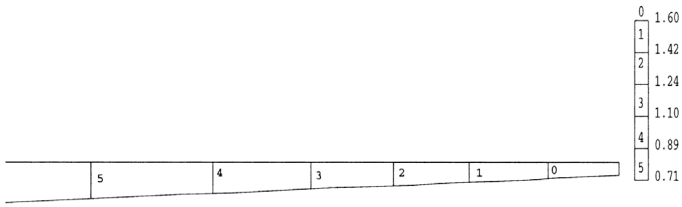

(c) Nip-region, pressure line contours (values*10^5), U_{roll} = 90% $\overline{U}_{foil}$

Figure 5.
a. Pressure and shear-rate line plots (values*10^3), increasing roll-speed b. Foil distributional pressure (P_f) values*10^3, towards the nip c. Pressure line contours (values *10^5), $U_{roll} = 90\%\ \bar{U}_{foil}$

$u_{roll}/\bar{U}_{foil}$	a_{inlet}	$\dot{\gamma}_{nip}$	P_{nip}	L_{foil}	D_{roller}
0.9	1.1	0.424E+00	0.160E+03	0.131E+04	0.131E+01
0.99	1.01	0.417E+00	0.155E+03	0.126E+04	0.136E+01
1.08	0.92	0.438E+00	0.151E+03	0.122E+04	0.142E+01
1.20	0.83	0.494E+00	0.147E+03	0.116E+04	0.149E+01

Table I.
Solution variation with roll-speed, values *10^3 units.

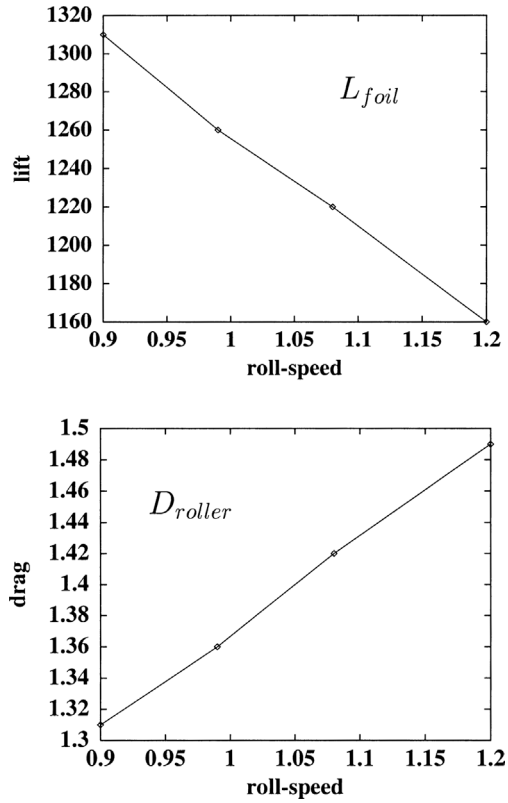

Figure 6.
Line plots, lift on foil and drag on roller (values $*10^3$), increasing roll-speed

the roller is $O(10^4)$ units and increases with increasing roll-speed, but remains three orders of magnitude lower in size than the lift. Hence, with increasing roll-speed, decreasing linear trends are observed in pressure and lift, and increasing trends in drag and shear-rate. It is not surprising that the lift on the foil decreases with increasing roller speed. As the roll-speed is increased, the foil-speed becomes smaller in comparison. Thus, the lift on the foil decreases with increasing roll-speed (or decreasing foil-speed). The variation in each quantity is noted in Table I, where a_{inlet} is the inlet layer thickness carried by the roller. We reiterate, outlet-coating thickness is maintained throughout at 1 unit.

Free-surface location and its adjustment with increasing roll-speed may be discerned from Figure 8 and is calibrated by the departure from the initial fixed location setting. These adjustments are noted to be only minor perturbations. The inflow feed decreases in thickness with increasing roll-speed, as the outlet strip-coating width is held fixed.

6.3 Analysis with increasing/decreasing foil-speeds

With the alternative series of adjustments based upon variation in foilspeeds, flow patterns in streamlines indicate a rise in vortex location with increase

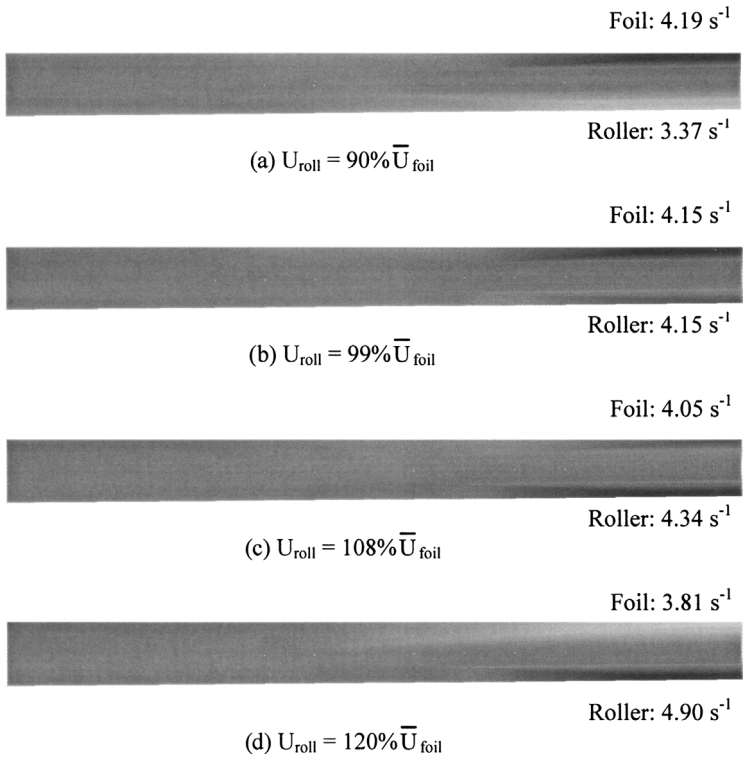

Figure 7.
Shear-rate contours (values $*10^2$), increasing roll-speed

in foil-speed, see Figure 9. Since flow rate is determined by the coat-oulet flow, increasing foil speed implies enhanced flow rate from one setting to another, presuming adjustment in pre-metering. The rising inflow rate at increasing foil-speeds, generates high pressures that push the vortex up towards the foil, see Figure 9b–e. Correspondingly, there is a drop in vortex location with decrease in foil-speed to $0.5\,\bar{U}_{\text{foil}}$, see Figure 9a. Distortion in the streamline patterns near the meniscus region is clearly apparent with increasing and decreasing foilspeeds. Meniscus shapes adjust accordingly. At fixed-strip coating width, the inflow thickness on the roller widens as foil-speed increases, see Figure 9b–e, and narrows with decreasing foil-speed, see Figure 9a.

In contrast to the scenario of increasing roll-speeds, here foil-pressures, nip shear-rates, foil-lift and roller-drag all demonstrate essentially linear increasing trends with increasing foil-speed, see Figure 10. This means that the levels of foilpressure, foil-lift and roller-drag double, with doubling of foil-speed. It is noticeable once more that lift on the foil is three orders of magnitude larger than that of drag on the roller. The corresponding results are charted in Table II. Figure 11 shows the foil-pressure distribution travelling towards the

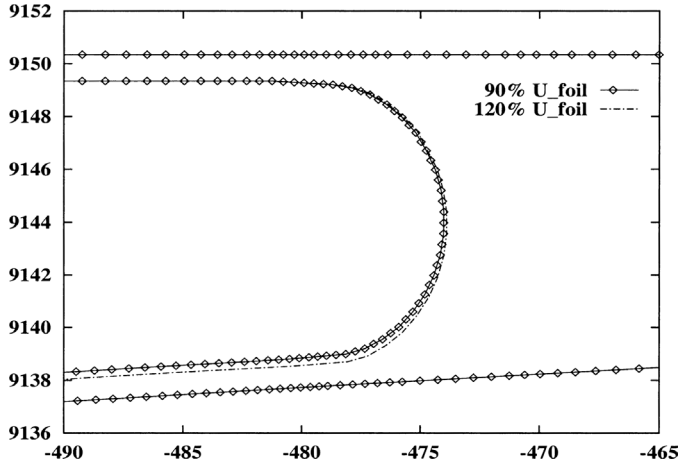

Figure 8.
Free-surface profiles, increasing roll-speed

nip-region. The level of pressure increases with increasing foil-speed raising the maximum nip-pressure level. In contrast to roller-speed variation, the region of maximum pressure is drawn towards the nip as foil-speed increases and pressure levels rise at the meniscus region, correspondingly. Limiting trends at both meniscus and nip are displayed in line contours of Figure 12, to associate the spatial distribution of pressure. The rising pressure at the nip with foil-speed is clearly evident by inspection in Figure 13. Here, the increase in foil-speed is more than twice the standard setting. For foil-speeds lower than roll-speeds, maximum shear-rates shift to the roller, see Figure 14, and pressure levels decline at the meniscus zone (Figure 12a).

6.4 Instability analysis: inlet flow on roller

Lastly, we consider flow response to variation in roller inflow. This is to identify flow sensitivity (coating outlet) to inlet flow perturbations. We note that the roller-inlet flow may inherit any flow disturbances generated, either from the pickup-metering roll or metering-applicator roll. To accomplish this a small sinusoidal wave (Carvalho and Scriven, 1997) is imposed at the free-surface inlet boundary on the roller and the full flow is solved up to the nip, meniscus and coating regions. As shown in Figure 3, no flow penetrates the flow zone internal to the meniscus free-surface region (recirculation region). Such sinusoidal disturbances die away, due to the presence of the roller-inlet and meniscus free-surfaces, see Figure 15. The crosssection velocity profiles are observed to merge into a plug flow form, similar to those in the standard setting (with absence of imposed inlet disturbances). Hence, plug flow patterns are resumed prior to the meniscus region. The freesurface setting has dissipated inlet oscillations, so that these do not influence the meniscus or

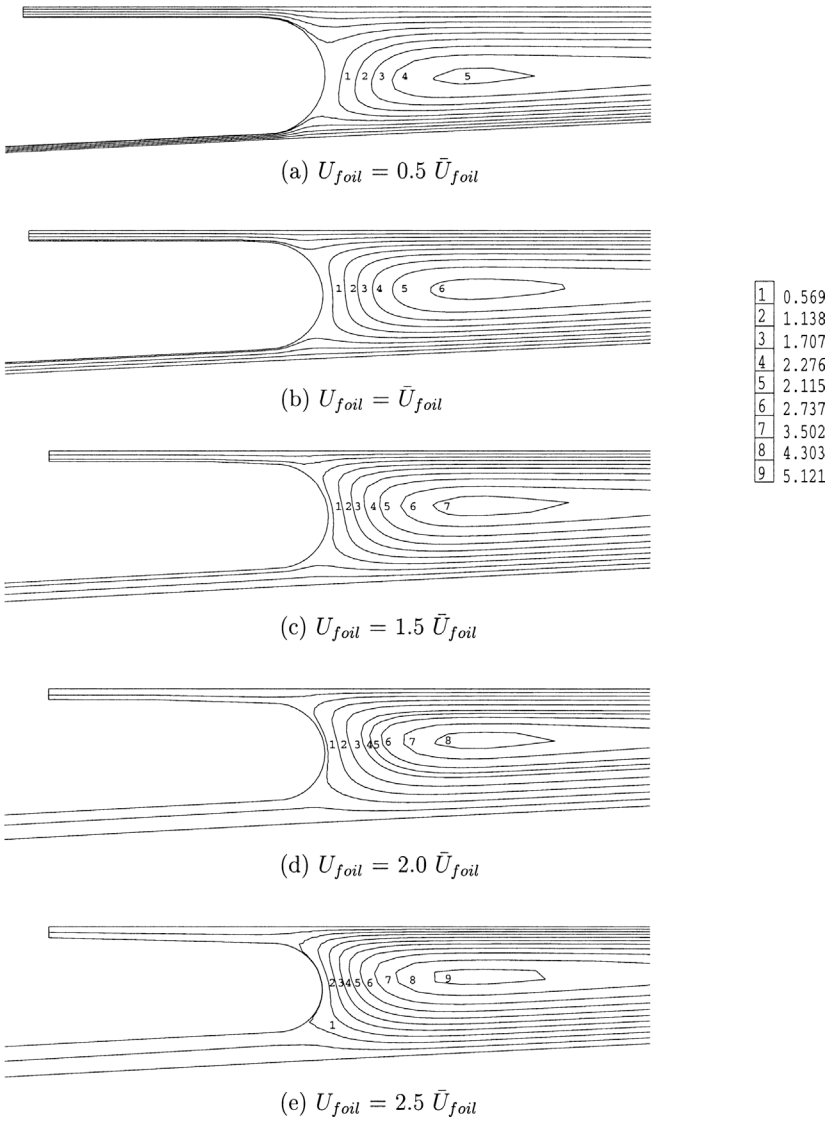

(a) $U_{foil} = 0.5\ \bar{U}_{foil}$

(b) $U_{foil} = \bar{U}_{foil}$

(c) $U_{foil} = 1.5\ \bar{U}_{foil}$

(d) $U_{foil} = 2.0\ \bar{U}_{foil}$

(e) $U_{foil} = 2.5\ \bar{U}_{foil}$

Figure 9.
Streamline patterns, increasing foil-speed

foil-coating flow structure. We illustrate these findings in Figure 15, on profiles and free-surface shapes, covering the zoomed section at the roller inlet alone. Fluid travels along the roller to the nip, the flow reverses at the nip-region and returns along the foil. We conclude that these influences do not affect the $\text{coat}_{\text{outlet}}$ flow.

On this evidence and under constant inflow due to pre-metering, it would appear reasonable to disregard roller inflow spatial instabilities, within the

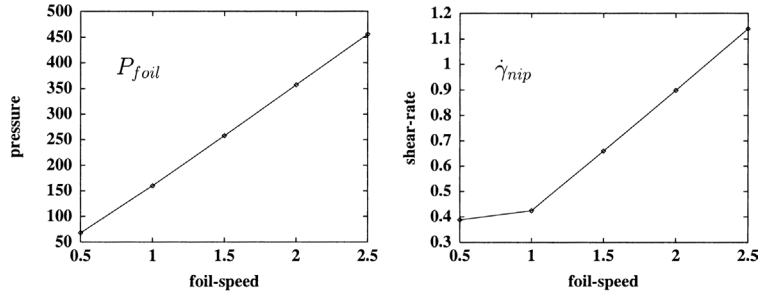

(a) Line plots, pressure and shear-rates (values*10^3), increasing foil-speed

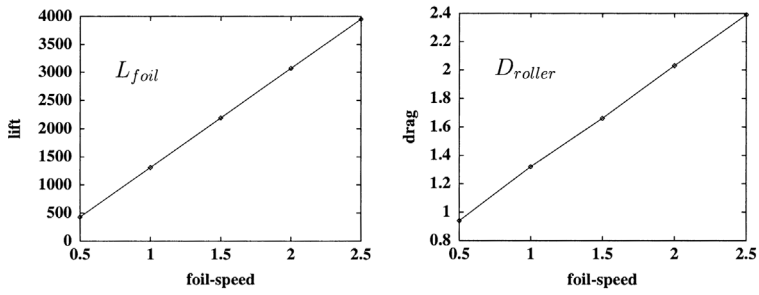

(b) Line plots, lift and drag (values*10^3), increasing foil-speed

Figure 10.
a. Line plots, pressure and shear-rates (values *10^3), increasing foilspeed, b. Line plots, lift and drag (values *10^3), increasing foil-speed

$u_{\text{foil}}/\bar{U}_{\text{foil}}$	a_{inlet}	$\dot{\gamma}_{\text{nip}}$	P_{nip}	L_{foil}	D_{roller}
0.5	0.55	0.388E+00	0.678E+02	0.427E+03	0.094E+01
1.0	1.1	0.424E+00	0.160E+03	0.131E+04	0.130E+01
1.5	1.6	0.660E+00	0.258E+03	0.219E+04	0.166E+01
2.0	2.2	0.898E+00	0.357E+03	0.307E+04	0.203E+01
2.5	2.7	0.114E+01	0.456E+03	0.395E+04	0.239E+01

Table II.
Solution variation with foil-speed, values *10^3 units.

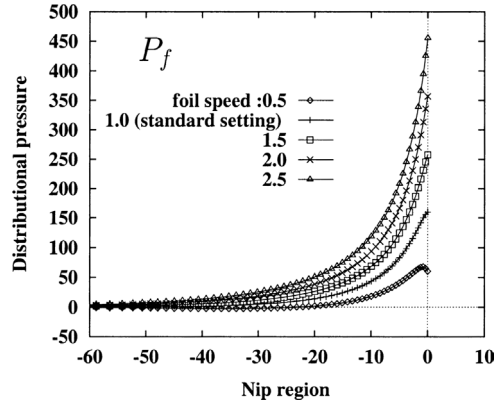

Figure 11.
Foil distributional pressure (values *10^3), towards nip, increasing foilspeeds

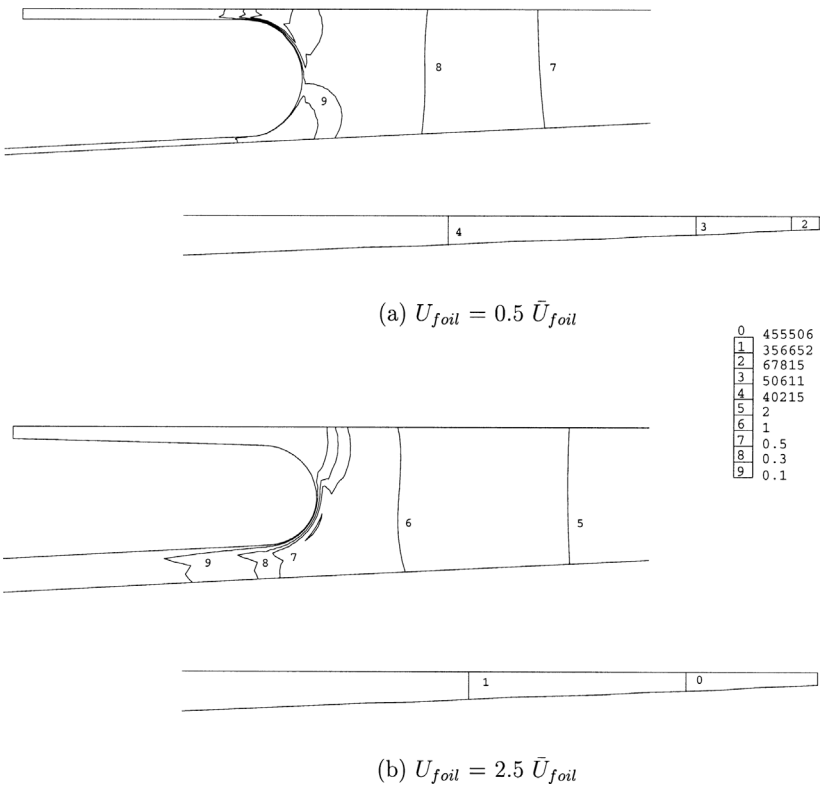

Figure 12.
Pressure line contours, meniscus-nip zones, increasing foil-speed

overall scheme of analysis. Flow adjustment at the nip and temporal instabilities remain outstanding.

7. Conclusions

A complex roller-coating problem of industrial relevance is analysed. The effects of increasing foil and roll-speeds on characteristic flow quantities such as pressure, lift, drag and shear-rate are reported. At increasing roll-speeds, pressure and lift on the foil display a linear decreasing trend, the levels of maximum field pressure broaden away from the nip and the location of maximum shear-rate shifts towards the roller. In contrast with increasing foil-speeds, a linear increasing trend is observed in foil-pressure and lift. Also the levels of maximum pressure migrate towards the nip and the location of maximum shear-rate switches towards the foil. As for drag on the roller, a linear increasing trend is observed with both increasing roller and foil speeds.

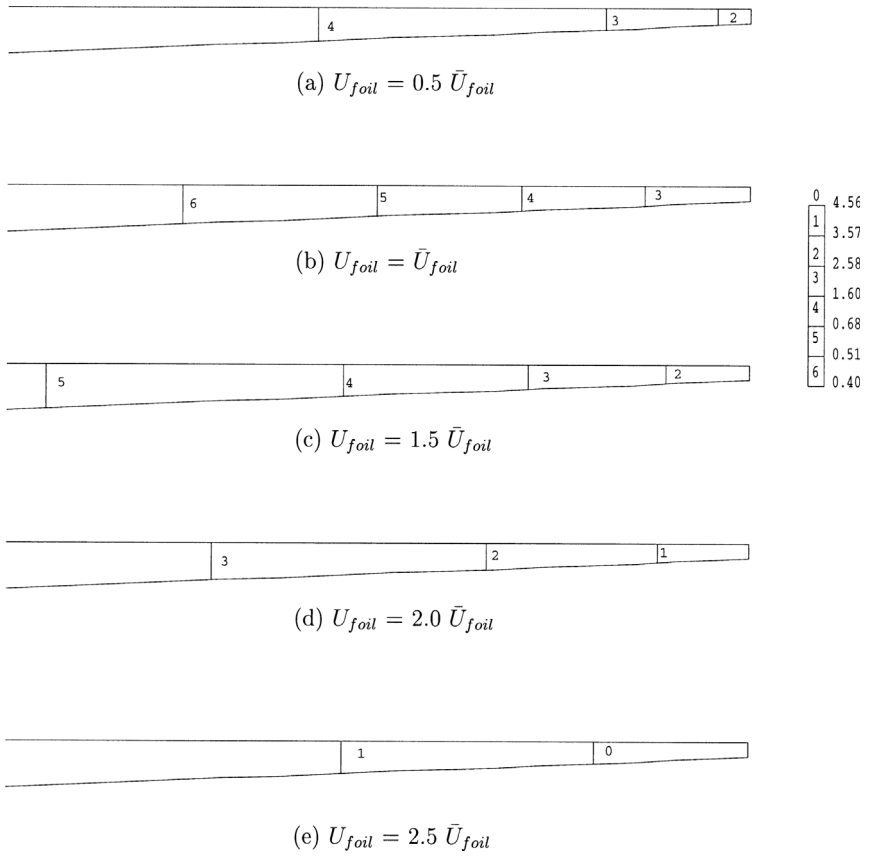

Figure 13.
Pressure line contours, nip zone; full range of foil speeds

Distorted streamline patterns are identified adjoining the meniscus upon increasing foil-speed. The higher the speed, the greater the streamline distortion in the direction of dominant flow (roller or foil speed). Vortex centres shift towards the foil at increasing foil-speed, and towards the roller at decreasing foil-speed. Any inherited flow disturbances generated, from the pickupmetering-applicator rollers, are not found to have any influence on the coatoutlet flow, due to the presence of the roller inlet and meniscus free-surfaces.

Significantly, no flow reversal is encountered around and in the vicinity of the free-surface meniscus. The lacquer coatings are essentially Newtonian in character. It is not surprising therefore that, linear trends are observed with parameter variation in the different quantities measured. As excess of lift above sheet weight may be equated unequivocally to vertical shift of foil position, hence it is conspicuous that flow instability is more likely to be

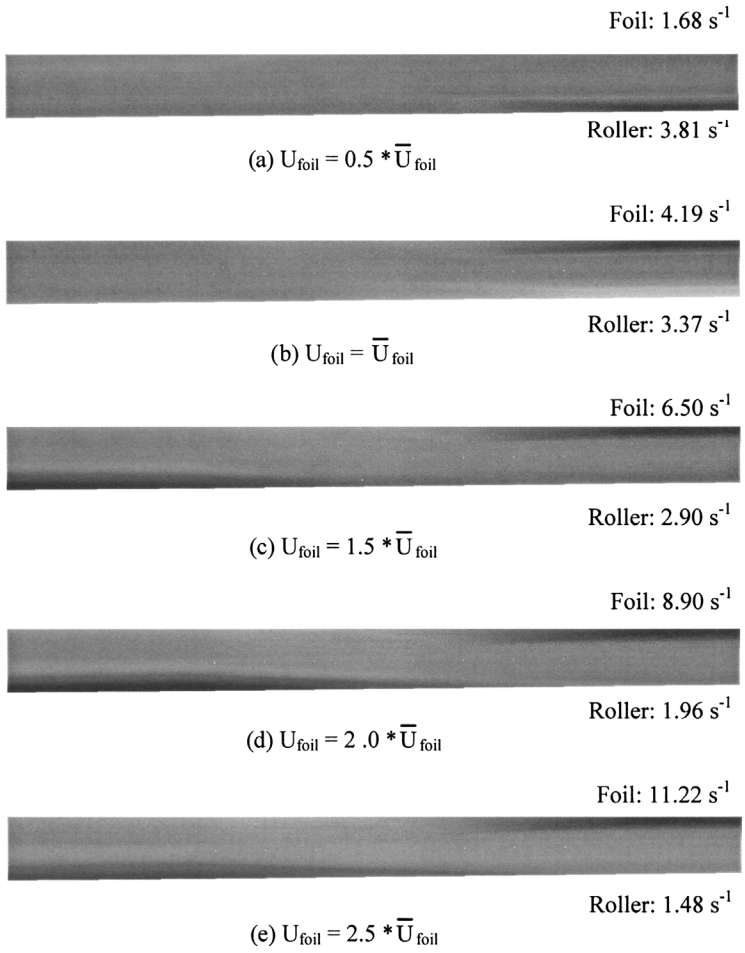

Figure 14.
Shear-rate contours (values $*10^2$), increasing foil-speed

stimulated by increase of foil-speed than that through roll-speed. The excessive build-up of pressure in the nip region (magnitude of 10^6 units), influences vortex flow structure and meniscus shapes. The elevated pressure in the nip, will force the foil to move vertically and relax the normal forces by creating a wider gap between roller and foil. This phenomenon, occurring in time, will create foil vibration and generate flow instabilities, subsequently giving rise to wavy patterns on the film coating (chatter and starvation, causing flow

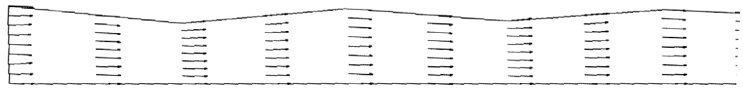

Figure 15.
Interior velocity fields at roller inlet

lines). Future studies are intended to focus on these temporal processing instabilities.

References

Benjamin, D.F. (1994), *Roll Coating Flows and Multiple Flow Systems*; PhD. Thesis, University of Minnesota, Minneapolis, MN, University Microfilms Int., Ann. Arbor, MI.

Carvalho, M.S. and Scriven, L.E. (1997a), "Multiple atates of a viscous free-surface flow: transition from pre-metered to a metering flow", *Int. J. Num. Meth. Fluids*, 24, pp. 813-31.

Carvalho, M.S. and Scriven, L.E. (1997), "Deformable foll coating flows: steady state and linear perturbation analysis", *J. Fluid Mech.*, 339, pp. 143-72.

Chen, K.S.A. and Scriven, L.E. (1988), *Roll Coating, Forward and Reverse: Effect of Feed Condition*, AIChE Spring Nat. Meet., New Orleans, LA.

Cohu, O. and Magnin, A. (1997), "Forward roll coating of Newtonian fluids with deformable rolls: an experimental investigation", *Chem. Eng. Sci.*, 52 No. 8, pp. 1339-47.

Carew, E.O.A., Townsend, P. and Webster, M.F. (1993), "A Taylor-Petrov-Galerkin algorithm for viscoelastic flow", *J. non-Newtonian Fluid Mech.*, 50, pp. 253-87.

Cuvelier, C., Segal, A., Van Steenhoven, A.A. (1986), *Finite Element Methods and Navier-Stokes Equations*, D. Reidel.

Ding, D., Townsend, P., Webster, M.F. (1993), *Numerical Simulation of Filling Problems Related to Injection Moulding*, Proceedings of IUTAM symposium on Numerical Simulation of non-isothermal flow of Viscoelastic Liquids, Netherlands.

Fourcade, E., Bertrand, F., Régalt, O. and Tanguy, P.A. (1999), "Finite element analysis of fluid-solid interaction in the metering nip of a metering size press", *Comp. Meth. Appl. Mech. Eng.*, 174, pp. 235-45.

Hawken, D.M., Tamaddon-Jahromi, H.R., Townsend, P. and Webster, M.F. (1990), "A Taylor-Galerkin based algorithm for viscous incompressible flow", *Int. J. Num. Meth. Fluids*, 10, pp. 327-51.

Hirt, C.W., Amsden, A.A. and Cook, J.L. (1974), "An arbitrary Lagrangian-Eulerian computing method for all flow speeds", *J. Comp. Phys.*, 14, pp. 227-53.

Isaksson, P. and Rigdahl, M. (1994), "Numerical simulation of blade coating with short dwell and roll application coaters", *Rheo. Acta*, 33, pp. 454-67.

Keunings, R. (1986), "An algorithm for the simulation of transient visco-elastic flows with free-surfaces", *J. Comp. Phys.*, 62, pp. 199-220.

Nithiarasu, P. and Zienkiewicz, O.C. (2000), "On stabilization of the CBS algorithm: Internal and external time steps", *Int. J. Num. Meth. Eng.*, 48, pp. 875-80.

Ramaswamy, B. (1990), "Numerical simulation of unsteady viscous free-surface flow", *J. Comp. Phys.*, 90, pp. 396-430.

Regalt, O., Labrie, R. and Tanguy, P.A. (1993), "Free-surface model for dip coating process", *J. Comp. Phys.*, 109, pp. 238-46.

Saito, H. and Scriven, L.E. (1981), "Study of coating flow by the finite element method", *J. Comp. Phys.*, 42, pp. 53-76.

Sato, T. and Richardson, S.M. (1994), "Numerical simulation method for viscoelastic flows with free surface-fringe element generation method", *Int. J. Num. Meth. Fluids*, 19, pp. 555-74.

Silliman, W.J. and Scriven, L.E. (1980), "Separating flow near a static contact line: slip at a wall and shape of a free surface", *J. Comp. Phys.*, 34, pp. 287-313.

Sizaire, R. and Legat, V. (1997), "Finite element simulation of a filament stretching extensional rheometer", *J. non-Newtonian Fluid Mech.*, 71, pp. 89-107.

Tanner, R.I., Nickell, R.E. and Bilger, R.W. (1975), "Finite element method for the solution of some imcompressible non-Newtonian fluid mechanics problems with free surfaces", *Comp. Meth. App. Mech. Eng.*, 6, pp. 155-74.

Townsend, P., Webster, M.F. (1987), *An Algorithm for the Three-Dimensional Transient Simulation of non-Newtonian Fluid Flows*, Proc. NUMETA 87, Martinus Nijhoff, Dordrecht, vol. 2 T12/1.